Supplementary Information

Optomechanical measurement of thermal transport in two-dimensional $MoSe_2$ lattices

Section 1 – Characterization of $MoSe_2$ Monolayers

We select $MoSe_2$ monolayers using optical microscopy measurements for the fabrication of devices. We use low-temperature photoluminescence measurements to confirm that fabricated devices consist of monolayer flakes (Fig. S1). The spectrum shows the exciton and the trion peaks.

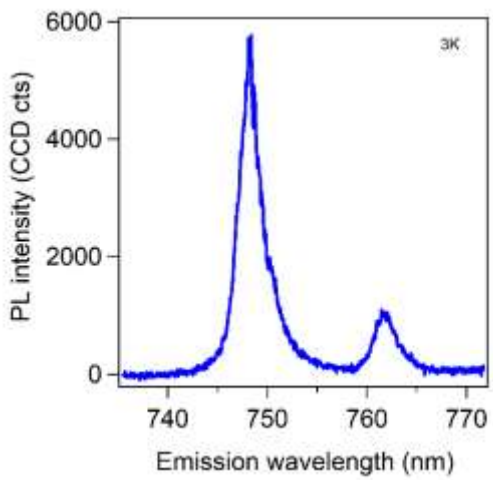

Figure S1: Photoluminescence spectrum of the $MoSe_2$ monolayer used to fabricate the 2.5 μm radius drum discussed in the main text. The spectrum is recorded using a HeNe laser with 20 μW power. The background of the spectrum is substracted.

Section 2 – Absorption of suspended $MoSe_2$ monolayers

The intensity of the laser oscillates as a function of the coordinate in the direction perpendicular to the substrate surface because of the interference between the incident and the reflected beam. Figure S2 shows the calculated intensity profile $I(z)$ normalized to the intensity I_0 of the incident beam for our device layout. The oscillation of I/I_0 is limited between 0.4 and 1.3 because of the absorption of the Si substrate. The intensity of the beam is $0.5 \cdot I_0$ at the level of the monolayer. The intensity profile in Fig. S2 is obtained using the Lumerical FDTD full wave simulation. We use 5.7 % for the absorption coefficient from the measurements in Ref. [1]. Overall, we have that the absorbed laser power is $P = 0.5 \cdot 0.057 \cdot P_0$ where P_0 is the measured power of the incident laser.

We verify that the absorption of $MoSe_2$ monolayers at 633 nm remains constant when varying the temperature from 3 to 300 K and when sweeping the gate voltage from – 4 V to +4 V. We carry out the measurements on $MoSe_2$ monolayers transferred on Si chips. We study the absorption by comparing the measured reflection power when the laser beam is focused on the $MoSe_2$ monolayer and when it is focused nearby the monolayer.

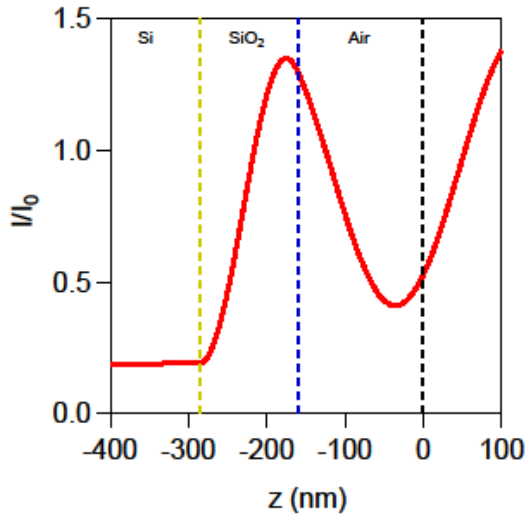

Figure S2: Simulated intensity profile of the normalised laser intensity in the direction perpendicular to the substrate. The black dashed line at $z = 0\ nm$ corresponds to the position of the monolayer. The wavelength of the laser beam is 633 nm. The oxide thickness is 125 nm and the air gap is 160 nm; these values are obtained from ellipsometry and atomic force microscopy measurements.

Section 3 – Membrane under tension

We carry out optomechanical experiments on stretched membranes. We estimate the strain from the measured dependence of the resonant frequency on the gate voltage shown in Fig. S3 using the following expression

$$f_{\mathrm{m}}\left(V_{\mathrm{g}}^{\mathrm{dc}}\right) = \frac{1}{2\pi}\sqrt{\frac{4.29E_{2\mathrm{D}}}{m_{\mathrm{eff}}}\epsilon - \frac{0.271}{m_{\mathrm{eff}}}\frac{\epsilon_0 \pi R_0^2}{d^3}\left(V_{\mathrm{g}}^{\mathrm{dc}} - \Delta\phi\right)^2}. \qquad \text{(S1)}$$

Here $E_{2\mathrm{D}}$ corresponds to the two dimensional young modulus of $MoSe_2$, R_0=2.5 μm is the radius of the resonator, d=200 nm is the effective distance between the gate and the membrane (taking into account the dielectric constant of the substrate), and $\Delta\phi$ is the work function difference between the gate electrode and the resonator. We obtain the effective mass m_{eff} from the curvature of the parabola. We then estimate the strain ϵ from the resonant frequency at $V_{\mathrm{g}}^{\mathrm{dc}} = \Delta\phi$ [2]. In all our $MoSe_2$ drums we obtain a positive strain in the range $0.1 - 1\%$. The fact that our drums are under tension is confirmed by the strong temperature dependence of the resonant frequency shown in Fig. 2c of the main text. The latter behavior is attributed to the thermal contraction of the $MoSe_2$ crystal when lowering temperature [2]. The positive strain at room temperature arises from the built-in stress created during fabrication [2].

These measurements show that the membrane is flat when $\Delta V_{\mathrm{g}}^{\mathrm{dc}} = (V_{\mathrm{g}}^{\mathrm{dc}} - \Delta\phi) \simeq 0$, while it becomes bent at finite $\Delta V_{\mathrm{g}}^{\mathrm{dc}}$ due to the electrostatic force. We estimate that the central position of our drums is deflected by $\lesssim 10\ \mathrm{nm}$ when $\Delta V_{\mathrm{g}}^{\mathrm{dc}} = 4V$. Figure S3 shows that $\Delta\phi \simeq 0.2\ \mathrm{V}$ for the 2.5 μm radius drum discussed in the main text.

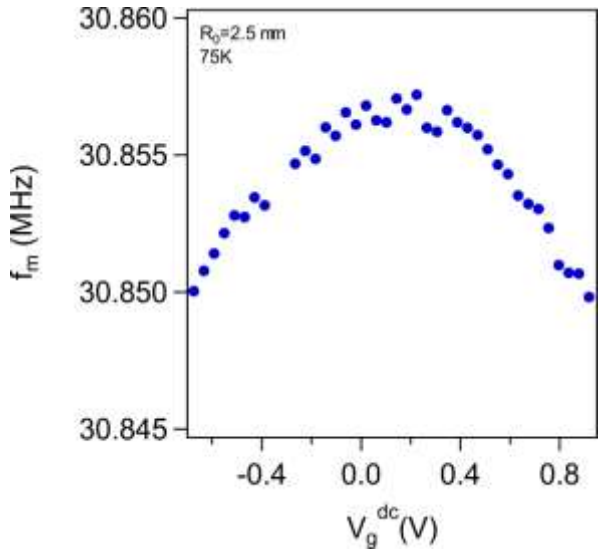

Figure S3. Mechanical resonance frequency as a function of static gate voltage.

Section 4 – measurements of the equivalent thermal conductance and the equivalent heat capacity

Raman measurements of the equivalent thermal conductance published in previous works

The thermal conductivity of graphene and other 2D materials has been intensively studied with Raman measurements [1,3-9]. The device consists typically of a suspended monolayer disc clamped at its edge. A gradient of temperature ΔT is produced between the center of the membrane and its circular edge using a focused laser beam. The heat flow is given by the laser power ΔP absorbed in the membrane (Fig. S4a). It is assumed that the absorbed energy is transferred to the phonons of the membrane. The temperature at the center of the membrane is probed by measuring the shift of the Raman-peak frequency when sweeping the laser power, which gives $\delta f_R/\delta P$. The temperature variation is calibrated by measuring the Raman-peak frequency as a function of the temperature of the setup, that is, $\delta f_R/\delta T$. The thermal conductance K is:

$$K = \frac{\Delta P}{\Delta T} = \frac{\delta f_{\mathrm{R}}/\delta T}{\delta f_{\mathrm{R}}/\delta P}. \qquad \text{(S2)}$$

This Raman method to study thermal conductance of two dimensional materials has been used with great success at room temperature by many groups [1,3-9]. However, this method is not suitable at cryogenic temperatures, since the frequency shift of the Raman peak is typically resolved with laser powers of the order of 100 μW or above, which leads to significant absorption heating. We show in this work that this problem is overcome using the resonant peak of the fundamental acoustic mode of the membrane. The quality factor of this mode increases by nearly three orders of magnitude when lowering temperature from 300 K to 3.5 K [2], so that the peak is resolved with low laser powers and without absorption heating.

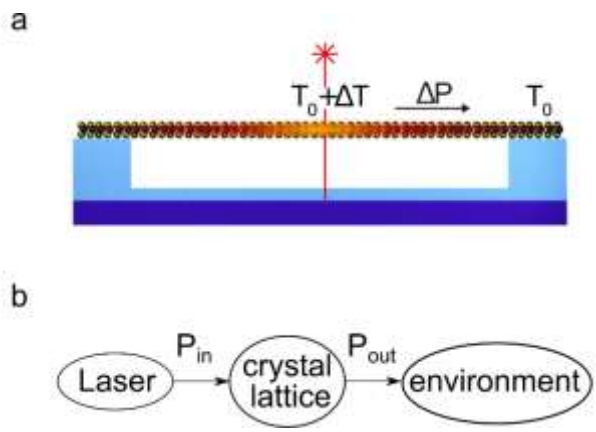

Figure S4: (a) Monolayer membrane coupled to a focused laser beam. The laser acts as a local heat source. The heat travels through the monolayer crystal from the center of the crystal to its circular clamping edge. Because of the thermal resistance, the heat flow ΔP leads to a temperature gradient ΔT. The yellow region corresponds to higher temperature, while red black regions correspond to lower temperature. (b) Schematic of the power flow. The power P_{in} flowing into the monolayer crystal is equal to the power P_{out} flowing out the crystal.

Optomechanics measurement of the equivalent thermal conductance

Our method is based on the measurement of the fundamental vibrational mode of the suspended membrane, namely the lowest energy flexural mode, instead of the Raman mode. We measure the shift of the resonant frequency when the absorbed laser power P is increased in order to get $\frac{\delta f_{\mathrm{m}}}{\delta P}$. We assume that the absorbed energy is entirely transferred into the phonon modes of the crystal as in the Raman method. As a calibration, we measure the resonant frequency as a function of the temperature of the cryostat, that is, $\frac{\delta f_{\mathrm{m}}}{\delta T}$. We obtain the equivalent thermal conductance

$$K = \frac{\Delta P}{\Delta T} = \frac{\delta f_{\mathrm{m}}/\delta T}{\delta f_{\mathrm{m}}/\delta P}. \qquad \text{(S3)}$$

The resonant frequency depends on the temperature because of the thermal expansion of the $MoSe_2$ crystal [2]. Here, ΔT is an effective temperature that depends on the temperature profile over the entire suspended monolayer, as we will see in Section 5.

Optomechanics measurement of the heat transport time

There is a static and a dynamical backaction of the laser beam on the dynamics of the resonator. The static backaction is a simple absorption heating effect that increases the temperature of the resonator as discussed above. It shifts the resonant frequency by Δf_{T} and the damping rate by $\Delta \Gamma_{\mathrm{T}}$. The dynamical backaction is related

to the retardation of the photothermal force [10]. Here, the absorption heating expands the $MoSe_2$ crystal, which is equivalent to a force. The displacement dependence of the absorbed power laser is not constant because of the interference pattern of the laser intensity in the direction perpendicular to the substrate (Fig. S2). In the course of one period of the displacement oscillation, the absorbed laser power oscillates as well. Because the membrane takes a finite time to heat up or to cool down, the photothermal force oscillates with a finite phase shift compared to the displacement oscillation. The in-phase photothermal force modifies the resonant frequency by Δf_{B} and the out-of-phase photothermal force modifies the damping rate by $\Delta \Gamma_{\mathrm{B}}$,

$$\Delta\left(f_{\mathrm{B}}^2\right) = -f_{\mathrm{m}}^2 \frac{dF}{dz}\frac{1}{k}\frac{1}{1+(2\pi f_{\mathrm{m}})^2\tau^2}, \tag{S4}$$

$$\Delta \Gamma_{\mathrm{B}} = \Gamma_{\mathrm{m}} Q \frac{dF}{dz}\frac{1}{k}\frac{2\pi f_{\mathrm{m}}\tau}{1+(2\pi f_{\mathrm{m}})^2\tau^2}, \tag{S5}$$

$$\tau = -\frac{\Delta\Gamma_{\mathrm{B}}}{4\pi f_{\mathrm{m}}\Delta f_{\mathrm{B}}}, \tag{S6}$$

with $\frac{dF}{dz} \propto P$ and $Q = \frac{f_{\mathrm{m}}}{\Gamma_{\mathrm{m}}}$. The retardation time given by τ corresponds to the time that takes the heat to travel from the center of the membrane to its circular edge.

Dynamical backaction in our device layout can be controlled with the voltage applied to the backgate of the wafer. The backaction force vanishes to zero for zero gate voltage when the membrane is flat, because the photothermal force is perpendicular to the displacement (Fig. S5).

Since the static and the dynamical backactions vanish to zero at zero laser power, we linearize the measured frequency f_{m} and damping rate Γ_{m} as functions of absorbed laser power P (Fig. S6).

$$f_{\mathrm{m}}(P) = f_{\mathrm{m}}(P=0) + aP, \tag{S7}$$

$$\Gamma_{\mathrm{m}}(P) = \Gamma_{\mathrm{m}}(P=0) + bP. \tag{S8}$$

At $\Delta V_{\mathrm{g}} \simeq 0\mathrm{V}$ there is static backaction, but no dynamical backaction (Figure S5),

$$\Delta f_{\mathrm{T}}(P) = a_{0V}P, \tag{S9}$$

$$\Delta \Gamma_{\mathrm{T}}(P) = b_{0V}P. \tag{S10}$$

At $\Delta V_{\mathrm{g}} = 4\mathrm{V}$ there are both static and dynamical backactions (Figure S5),

$$\Delta f_{\mathrm{T}}(P) + \Delta f_{\mathrm{B}}(P) = a_{4V}P, \tag{S11}$$

$$\Delta \Gamma_{\mathrm{T}}(P) + \Delta \Gamma_{\mathrm{B}}(P) = b_{4V}P. \tag{S12}$$

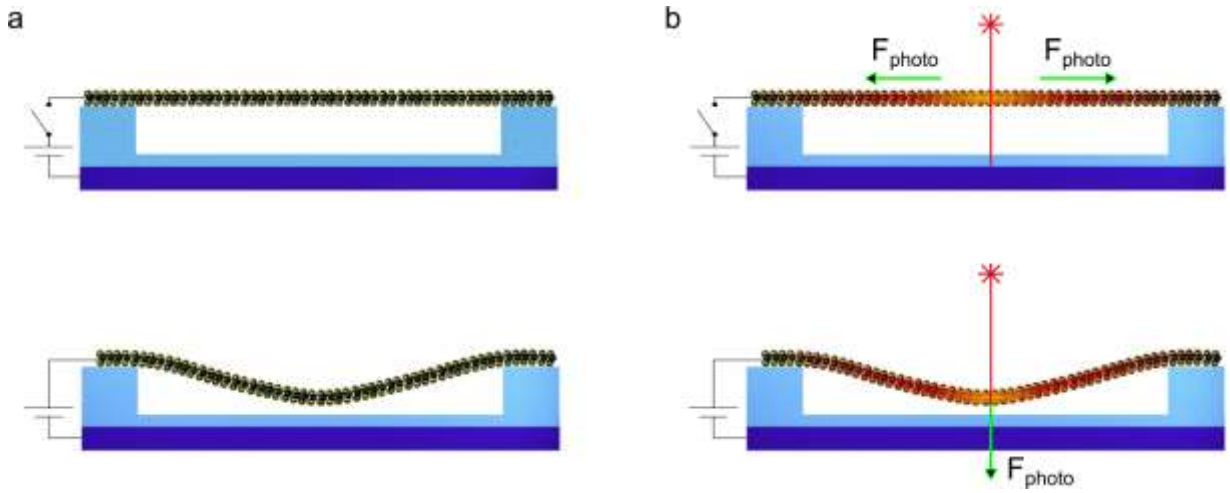

Figure S5: Cross section of the suspended monolayer membrane coupled to the laser beam. (**a**) At $\Delta V_g^{dc} \simeq 0$ the membrane is flat, while a finite gate voltage deflects the membrane. (**b**) When the membrane is flat, the dynamical backaction is suppressed to zero. Indeed, the thermal expansion of the crystal results in a force that cannot drive flexural vibrations. The force is perpendicular to the displacement. When the membrane is bent with a finite gate voltage, the dynamical backaction becomes finite, because the photothermal force can drive the resonator.

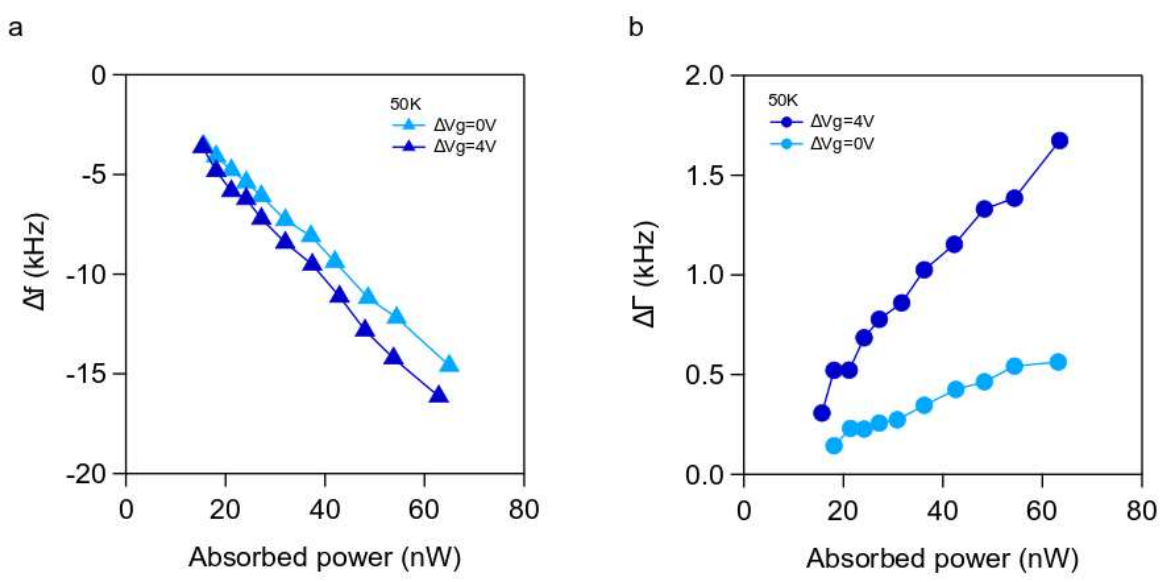

Figure S6: Measured variations of the resonant frequency **(a)** and damping **(b)** as functions of laser power for two different gate voltages. The dynamical backaction force is finite at $\Delta V_g^{dc} = 4\ V$, while is suppressed to zero at $\Delta V_g^{dc} \simeq 0\ V$, see Fig. S5.

The static dynamical backaction is expected to weakly change when varying the gate voltage by a few volts, because the static displacement remains small. As a result,

$$\Delta f_{\mathrm{B}}(P) = a_{0V}P - a_{4V}P, \tag{S13}$$

$$\Delta \Gamma_{\mathrm{B}}(P) = b_{0V}P - b_{4V}P, \tag{S14}$$

$$\tau = -\frac{b_{0V} - b_{4V}}{4\pi f_0(a_{0V} - a_{4V})}. \tag{S15}$$

Measurement of the equivalent heat capacity

The thermal transport in our experiment can be seen as the unidirectional flow of energy from the laser beam into the monolayer membrane in a first step, and from the membrane to the environment in a second step (Fig. S4b). We assume that all energy absorbed into the membrane flows to the environment via the phononic states of the crystal – this is the assumption made in the Raman measurements of thermal transport [1,3-9]. Because of the conservation of the heat flow, the power P_{in} flowing into the monolayer crystal is equal to the power P_{out} flowing out of the crystal. Here, P_{in} is the absorbed power P of the laser, and P_{out} is related to the heat-induced energy shift $\Delta E_{\mathrm{monolayer}}$ (stored in the monolayer crystal) multiplied by the energy escape rate $1/\tau$. This rate is given by the inverse of the measured characteristic time τ for the crystal to heat or to cool down. We have

$$P_{\mathrm{in}} = P, \tag{S16}$$

$$P_{\mathrm{out}} = \frac{\Delta E_{\mathrm{monolayer}}}{\tau}. \tag{S17}$$

Setting $P_{\mathrm{in}} = P_{\mathrm{out}}$, we define the equivalent heat capacity

$$C = \frac{\Delta E_{\mathrm{monolayer}}}{\Delta T} = \tau \cdot K \tag{S18}$$

with $K = P/\Delta T$ being the thermal conductance (Eq. S3). As noted above, ΔT is an effective temperature that depends on the temperature profile over the suspended monolayer. As a result, the equivalent heat capacity C differs by a constant β from the usual heat capacity of the membrane evaluated with a temperature that is uniform over the entire material. In Section 5, we show that β is about one in the ballistic regime and for our drum geometry.

Section 5 – Estimating the thermal conductivity and the specific heat capacity, predictions based on first-principles

Reminder – Relation between the conductance and the conductivity in previous Raman measurements

The thermal conductivity κ is inferred from K using the heat diffusion equation, as introduced in Ref. [4]. The laser is assumed to be a Gaussian beam with radius r_0. We have

$$\kappa = K\frac{\eta}{2\pi t} \tag{S19}$$

where t is the thickness of the $MoSe_2$ monolayer and η is a constant of the order of unity, which depends on the temperature profile along the radial coordinate r. The spatial temperature rise induced by the absorbed laser power variation ΔP is given by

$$\Delta T(r) = \frac{\Delta P}{2\pi\kappa t}\ln\left(\frac{R_0}{r}\right)\gamma(r) \tag{S20}$$

with

$$\gamma(r) = 1 + \frac{\mathrm{Ei}\left(-\frac{r^2}{r_0^2}\right) - \mathrm{Ei}\left(-\frac{R_0^2}{r_0^2}\right)}{2\ln\left(\frac{R_0}{r}\right)}. \tag{S21}$$

Here t is the thickness of the membrane and Ei is the exponential integral function. The edge of the drumhead is assumed to be well thermalized to the environment, so that $T(R = R_0) = T_0$ (Figure S4a). The temperature decreases logarithmically along r between r_0 and R_0.

Diffusive thermal transport – measured conductance and conductivity

We obtain the equivalent thermal conductance $K = \Delta P/\Delta\mathrm{T}$ by measuring the resonance frequency of the vibrational mode of the membrane as a function of the absorbed laser power and the cryostat temperature, as described in Section 4. The resonant frequency depends on the temperature because of the thermal expansion of the $MoSe_2$ crystal [2]. Here, ΔT is an effective temperature that depends on the temperature profile over the entire suspended monolayer, as we will see next. For small temperature changes of the cryostat, we can assume the thermal expansion coefficient α_T to be constant. The thermal expansion of the silicon substrate is comparatively negligible [2] and will be ignored below. In this case, it is straightforward to show (see for instance Ref. [11]) that for a circular membrane under initial uniform stress σ_0 at a uniform temperature T_0 the new tensile stress in the membrane for a radial non-uniform profile $T(r) = T_0 + \Delta T(r)$ is given by

$$\sigma_{\mathrm{rr}}(r) = \sigma_0 - \frac{\alpha E_{2\mathrm{D}}}{r^2}\int_0^r dr' r' \Delta T(r') - \frac{\alpha E_{2\mathrm{D}}}{R_0^2}\frac{1-\nu}{1+\nu}\int_0^{R_0} dr' r' \Delta T(r'), \tag{S22}$$

$$\sigma_{\theta\theta}(r) = \sigma_0 + \frac{\alpha E_{2D}}{r^2}\int_0^r dr' r' \Delta T(r') - \frac{\alpha E_{2D}}{R_0^2}\frac{1-\nu}{1+\nu}\int_0^{R_0} dr' r' \Delta T(r'), \tag{S23}$$

where σ_{ij} are the 2D stresses in polar coordinates (r, θ) and ν the Poisson's ratio of the material. Solving the wave equation and treating the nonuniform stress from the heating to lowest order in perturbation theory, one finds the frequency shift of the fundamental mode to be

$$\frac{\delta f_{\mathrm{m}}}{f_{\mathrm{m}}} = -\frac{\alpha_T}{2\epsilon}\left([1+\nu]\int_0^1 dx\, x\Delta T(x) + \frac{2(1-\nu)}{|J_1(\xi_{01})|^2}\int_0^1 dx \int_0^x \frac{dx' x'}{x} J_1(\xi_{01}x)^2 \Delta T(x')\right). \tag{S24}$$

Here, J_1 is the Bessel function of the first kind and $\xi_{01} \approx 2.40$ the first zero of J_0. The radial temperature profile ΔT has further been scaled to lie on the unit disc, and ϵ is the strain in the membrane at constant temperature T_0. We assume that the membrane at its clamping edge is thermalized to the environment, a good assumption for large diameter transition metal dichalcogenide monolayer membranes as demonstrated by Yan and coworkers [5].

In the diffusive regime, the spatial temperature rise induced by the absorbed laser power variation δP is given by

$$\delta T(x) = \frac{\delta P}{2\pi\kappa t}\left[\ln\left(\frac{1}{x}\right) + \frac{\mathrm{Ei}(-\gamma_0^2 x^2) - \mathrm{Ei}(-\gamma_0^2)}{2}\right], \tag{S25}$$

with $\gamma_0 = R_0/r_0$ [4,5]. In this work, the drum radius R_0 is either 1.5 or 2.5 μm, and r_0 is 0.35 μm. This allows us to quantify the thermal conductivity via the measured frequency shift of the membrane when illuminated by the laser. Upon combining Eqs. (S24) and (S25) we have

$$\frac{\delta f_{\mathrm{m}}}{\delta P} = -\frac{\alpha_T}{2\epsilon}\frac{f_{\mathrm{m}}}{2\pi\kappa t}\eta. \tag{S26}$$

We obtain the numerical factor $\eta \cong 0.64 + 0.02(\mathrm{r}_0/R_0) - 1.08(\mathrm{r}_0/R_0)^2 + 0.64(\mathrm{r}_0/R_0)^3$ from numerical integration of the expressions (S24) and (S25) using $\nu = 0.2$. We have $\eta = 0.62$ for the 2.5 μm drum and $\eta = 0.6$ for the 1.5 μm drum. The Poisson's ratio is given by $\nu = 1 - 2(\mathrm{v_t}/\mathrm{v_l})^2$ for a two-dimensional membrane. First principles computation results in $\mathrm{v_t} = 2774\ \mathrm{m/s}$ and $\mathrm{v_l} = 4391\ \mathrm{m/s}$ for the transverse and the longitudinal sound velocity of $MoSe_2$ monolayers, respectively.

From the calibration measurement of the frequency shift as a function of cryostat temperature (uniform temperature and membrane expansion) we further have

$$\frac{\delta f_{\mathrm{m}}}{\delta T} = -\frac{\alpha_T f_{\mathrm{m}}}{2\epsilon} \tag{S27}$$

Thus, the in-plane thermal conductivity of the $MoSe_2$ is found from the expression

$$\kappa = \frac{\eta}{2\pi t}\frac{(\delta f_{\mathrm{m}}/\delta T)}{(\delta f_{\mathrm{m}}/\delta P)} = K\frac{\eta}{2\pi t}. \tag{S28}$$

Optomechanical measurements and Raman measurements result in a similar relation between κ and K in the diffusive regime (Eqs. S19 and S28) but with different η values. Here, t=0.65 nm is the thickness of the $MoSe_2$ monolayer.

Diffusive and ballistic conductivity computed from first-principles Boltzmann transport equation

Here we discuss the numerical evidence pointing to ballistic conduction in $MoSe_2$. First, we compute the diffusive thermal conductivity κ_{diff} of an infinitely large $MoSe_2$ by solving a first-principles Boltzmann transport equation with a variational approach [12,13], where we take into account thermal resistance due to three-phonon interactions [14] and isotopic scattering [15] (at natural isotope abundances).

Next, we compute the ballistic conductivity κ_{ball} of a finite sample of $MoSe_2$, where phonon scattering events are neglected, but the phonon mean free path is limited by the system size. To simplify the comparison, we study an infinitely wide system with transport along a finite length equal to L. As the anisotropy of the material is small, the transport direction is taken to be aligned with the crystal zig-zag direction. It can be shown [16] that thermal conductivity in such system is

$$\kappa_{\text{ball}} = \frac{1}{N_{\boldsymbol{q}} V_{\text{cell}}} \sum\nolimits_{\boldsymbol{q},s} C_{\boldsymbol{q},s} \left| v_{\boldsymbol{q},s}^{//} \right|^2 \frac{L}{2} \tag{S29}$$

where $|v_{\boldsymbol{q},s}^{//}|$ is the projection of the phonon group velocity along the thermal gradient; and the effective length of thermal transport is $\frac{L}{2}$.

Finally, we compare κ_{ball} to the conductivity κ_{finite} of a finite trench of $MoSe_2$ that takes into account both intrinsic phonon interactions and finite-size effects. In this case, we solve the Boltzmann transport equation with a variational approach, considering an effective scattering term equal to $\frac{2\left|v_{\boldsymbol{q},s}^{//}\right|}{L}$ in addition to intrinsic interactions.

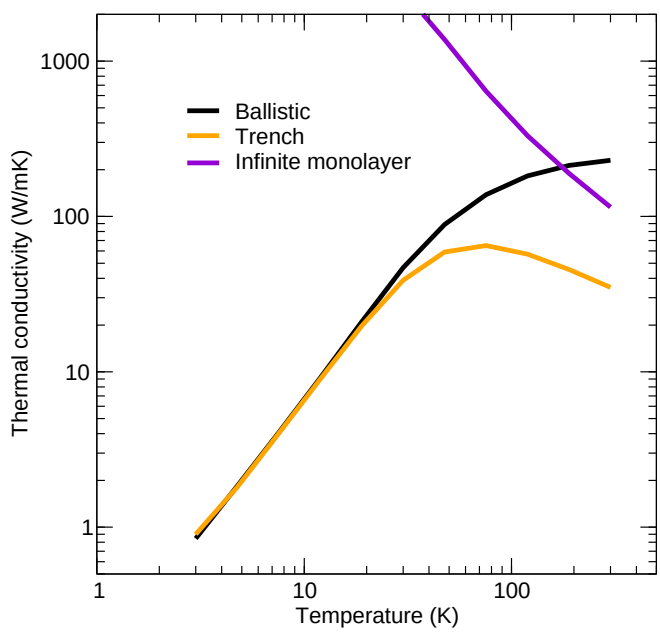

Figure S7: Computational comparison of the thermal conductivity of a finite-length $MoSe_2$ trench, the conductivity of an infinite $MoSe_2$ monolayer, and the conductivity in the ballistic limit of a finite-length $MoSe_2$ system. The conductivity of both the trench and the infinite monolayer includes intrinsic phonon scattering events.

In Fig. S7, we compare these three model conductivities for L =2.5 µm, i.e. a length comparable to the experimental sizes under examination. We observe that κ_{finite} below 100K is well approximated by the ballistic conductivity, which neglects any intrinsic phonon scattering event. Moreover, κ_{ball} is consistent with the measured temperature dependence of the conductivity. This rules out diffusive conduction. This result suggests that for the sizes considered in the experiment, intrinsic phonon interactions can be neglected and thermal transport can be described as a purely ballistic process at low temperatures.

We note that κ_{finite} is a rather simplistic interpolation between the ballistic and the diffusive limit, which fails to account for viscous effects arising from phonon interactions [17]. A more detailed discussion of such viscous effects would provide a more accurate representation of the crossover region between the ballistic and diffusive limit, particularly in the region around the thermal conductivity peak. To this aim, heat flux should be modeled by solving a set of coupled linear differential equations to obtain its radial and angular dependence. This task however, falls outside the purpose of this work and will be left for further studies. Nevertheless, we expect the qualitative features of κ_{finite} to be well described by the present modeling.

Ballistic thermal transport, thermal conductance, specific heat – relation between measurements and theory

We first note that the quantity $\delta f_{\mathrm{m}}/\delta T$ in Eq. S3 measured by changing the cryostat temperature corresponds to the case where the temperature remains constant over the membrane surface. However, the laser induces a spatially varying temperature profile over the membrane surface, whose precise shape depends on the conductance model, as will be discussed below. Since temperature is not uniform, the change of the resonance frequency $\left(\frac{\delta f_{\mathrm{m}}}{\delta T}\right)_{\mathrm{laser}}$ due to the laser heating differs from the change $\left(\frac{\delta f_{\mathrm{m}}}{\delta T}\right)_{\mathrm{cryo}}$ due to the cryostat temperature variation as

$$\left(\frac{\delta f_{\mathrm{m}}}{\delta T}\right)_{\mathrm{laser}} = \frac{1}{\alpha}\left(\frac{\delta f_{\mathrm{m}}}{\delta T}\right)_{\mathrm{cryo}}, \tag{S30}$$

where $\frac{1}{\alpha}$ is a scaling factor. We introduce K_{model} as

$$K_{\mathrm{model}} = \frac{\left(\frac{\delta f_{\mathrm{m}}}{\delta T}\right)_{\mathrm{laser}}}{\frac{\delta f_{\mathrm{m}}}{\delta P}} = \frac{\frac{1}{\alpha}\left(\frac{\delta f_{\mathrm{m}}}{\delta T}\right)_{\mathrm{cryo}}}{\frac{\delta f_{\mathrm{m}}}{\delta P}} = \frac{1}{\alpha}K \tag{S31}$$

which depends on the model used to predict the laser-induced profile of temperature. To compute the α factor for a given temperature profile $\delta T_{\mathrm{laser}}(r)$, we define an effective temperature T_{uniform} such that the frequency shift of the membrane for a constant temperature change $\delta T_{\mathrm{uniform}} = (T_{\mathrm{uniform}} - T_0)$ is the same as the frequency shift of a membrane for a non-uniform temperature change $\delta T_{\mathrm{laser}}(r)$.

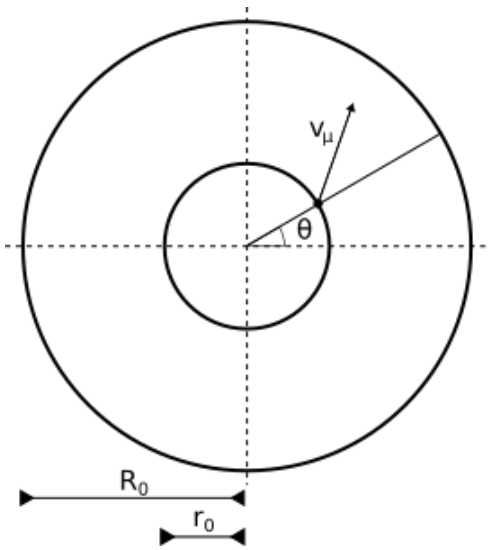

Next, we approximate the laser spot at the membrane center as an ideal heat reservoir with temperature T_{center}. We assume that transport takes place in absence of scattering events between the inner reservoir defined by the laser spot radius r_0 and the outer reservoir given by the drum radius R_0.

As a first step, we need a temperature profile to calculate α. Rigorously speaking, temperature cannot be defined in the ballistic regime, as phonons are not populated according to a Bose—Einstein distribution. Nevertheless, we can define a local temperature proportional to the number of excited phonons. To define the radial profile of temperature, we first note that the radial component of phonon velocities is constant, ensuring that the total heat flux flowing through a ring of radiuses r and $r + dr$, with $r_0 < r < R_0$, must be conserved. Therefore, the current density, and thus the phonon density, must decrease as $\frac{1}{r}$. As a result, the temperature profile of the membrane is:

$$T_{\text{laser}}(r) = T_0 + (T_{\text{center}} - T_0) \tag{S32}$$

for $r < r_0$; and

$$T_{\text{laser}}(r) = T_0 + \frac{r_0}{r}(T_{\text{center}} - T_0) \tag{S33}$$

for $r_0 < r < R_0$.

Taking into account the non-uniform stress as we did above, we find that $\frac{1}{\alpha}$ is well approximated by the relation:

$$\frac{1}{\alpha} = 2.45\frac{r_0}{R_0} - 1.9\left(\frac{r_0}{R_0}\right)^2 + 0.46\left(\frac{r_0}{R_0}\right)^3 \tag{S34}$$

Using r_0= 0.35 μm we find $\alpha = 2.1$ and $\alpha = 3.2$ for the 1.5 μm and 2.5 μm radius drum, respectively.

The conductance K_{model} can be obtained as follows. The contribution of a phonon to the heat flux at a point (r_0, θ) of the laser spot circumference (in polar coordinates) is:

$$\frac{1}{A_{\text{cell}}}\, r_0\, d\theta\, \bar{n}_{\boldsymbol{q},s}(T_{\text{center}})\, \hbar\omega_{\boldsymbol{q},s}\left(v^x_{\boldsymbol{q},s}\cos\theta + v^y_{\boldsymbol{q},s}\sin\theta\right) \quad \text{if } \left(v^x_{\boldsymbol{q},s}\cos\theta + v^y_{\boldsymbol{q},s}\sin\theta\right) > 0\,, \tag{S35}$$

for the phonons propagating out of the laser spot and

$$\frac{1}{A_{\text{cell}}} r_0 \, d\theta \, \bar{n}_{\boldsymbol{q},s}(T_0) \, \hbar\omega_{\boldsymbol{q},s} \left(v_{\boldsymbol{q},s}^x \cos\theta + v_{\boldsymbol{q},s}^y \sin\theta\right) \quad \text{if } \left(v_{\boldsymbol{q},s}^x \cos\theta + v_{\boldsymbol{q},s}^y \sin\theta\right) < 0 \,, \tag{S36}$$

for the phonons entering into the laser spot region. Here $\boldsymbol{q}$ is the phonon wavevector, s is the phonon branch index, $\bar{n}_{\boldsymbol{q},s}$ is the Bose—Einstein population, $\hbar\omega_{\boldsymbol{q},s}$ the phonon energy, $v_{\boldsymbol{q},s}^x \cos\theta + v_{\boldsymbol{q},s}^y \sin\theta$ is the projection of the phonon velocity in direction θ, A_{cell} is the unit cell area. Taking advantage of the invariance of the phonon energy upon momentum reversal, namely $\hbar\omega_{\boldsymbol{q},s} = \hbar\omega_{-\boldsymbol{q},s}$ and summing over phonon momenta and branches we obtain the heat flux current I:

$$I = \frac{2\pi r_0}{N_q \, A_{\text{cell}}} \sum_{\boldsymbol{q},s} \frac{\left(\bar{n}_{\boldsymbol{q},s}(T_{\text{center}}) - \bar{n}_{\boldsymbol{q},s}(T_0)\right)}{2} \hbar\omega_{\boldsymbol{q},s} \; \frac{1}{2\pi} \int_0^{2\pi} d\theta \left|v_{\boldsymbol{q},s}^x \cos\theta + v_{\boldsymbol{q},s}^y \sin\theta\right| = (T_{\text{center}} - T_0) \frac{2\pi r_0}{N_q \, A_{\text{cell}}} \sum_{\boldsymbol{q},s} \frac{C_{\boldsymbol{q},s}}{2} \frac{1}{2\pi} \int_0^{2\pi} d\theta \left|v_{\boldsymbol{q},s}^x \cos\theta + v_{\boldsymbol{q},s}^y \sin\theta\right| , \tag{S37}$$

where N_q is the number of $\boldsymbol{q}$-points, $C_{\boldsymbol{q},s} = \frac{\partial \bar{n}_{\boldsymbol{q},s}}{\partial T} \hbar\omega_{\boldsymbol{q},s}$ the phonon mode specific heat in J/K, and the factor 1/2 is used to consider in the sum only phonons propagating in the correct direction. The integral over θ can be evaluated as:

$$\frac{1}{2\pi} \int_0^{2\pi} d\theta \left|v_{\boldsymbol{q},s}^x \cos\theta + v_{\boldsymbol{q},s}^y \sin\theta\right| = \frac{1}{2\pi} \int_0^{2\pi} d\theta \left| |v_{\boldsymbol{q},s}| \cos v_{\boldsymbol{q},s}^{\phi} \cos\theta + |v_{\boldsymbol{q},s}| \sin v_{\boldsymbol{q},s}^{\phi} \sin\theta \right| = \frac{|v_{\boldsymbol{q},s}|}{2\pi} \int_0^{2\pi} d\theta \left|\cos(\theta - v_{\boldsymbol{q},s}^{\phi})\right| = \frac{2|v_{\boldsymbol{q},s}|}{\pi} , \tag{S38}$$

where in the second equality we wrote the phonon velocity in polar coordinates. Dividing the current I by $(T_{\text{center}} - T_0)$ we obtain the conductance K_{model} :

$$K_{\text{model}} = \frac{2\pi r_0}{N_q \, A_{\text{cell}}} \sum_{\boldsymbol{q},s} \frac{C_{\boldsymbol{q},s}}{2} \frac{2\left|v_{\boldsymbol{q},s}\right|}{\pi} . \tag{S39}$$

Finally, to compare with experiments, we take into account for the scaling factor α, so that the experimental equivalent conductance is evaluated as:

$$K = \alpha K_{\text{model}} = A_{\text{cross}} M, \tag{S40}$$

$$\mathrm{A}_{\text{cross}} = 2\pi r_0 t \alpha, \tag{S41}$$

$$M = \frac{\rho c v}{2} , \tag{S42}$$

$$c = \frac{1}{\rho t} \frac{1}{N_q A_{\text{cell}}} \sum_{\boldsymbol{q},s} C_{\boldsymbol{q},s} , \tag{S43}$$

$$v = \frac{1}{\sum_{\boldsymbol{q},s} C_{\boldsymbol{q},s}} \sum_{\boldsymbol{q},s} C_{\boldsymbol{q},s} \frac{2\left|v_{\boldsymbol{q},s}\right|}{\pi} , \tag{S44}$$

where we separated the conductance into a geometrical effective cross-section A_{cross} , which depends on t, r_0 and R_0 (Eq. S34), and a microscopic component M, explicitly indicating the specific heat capacity c in $\frac{\mathrm{J}}{\mathrm{K \cdot kg}}$ and the

average phonon radial velocity v. In Figure S8 and S9, we plot c and v as a function of temperature. We use t=0.65 nm for the thickness of the $MoSe_2$ monolayer and $\rho = 6900\ kg/m^3$.

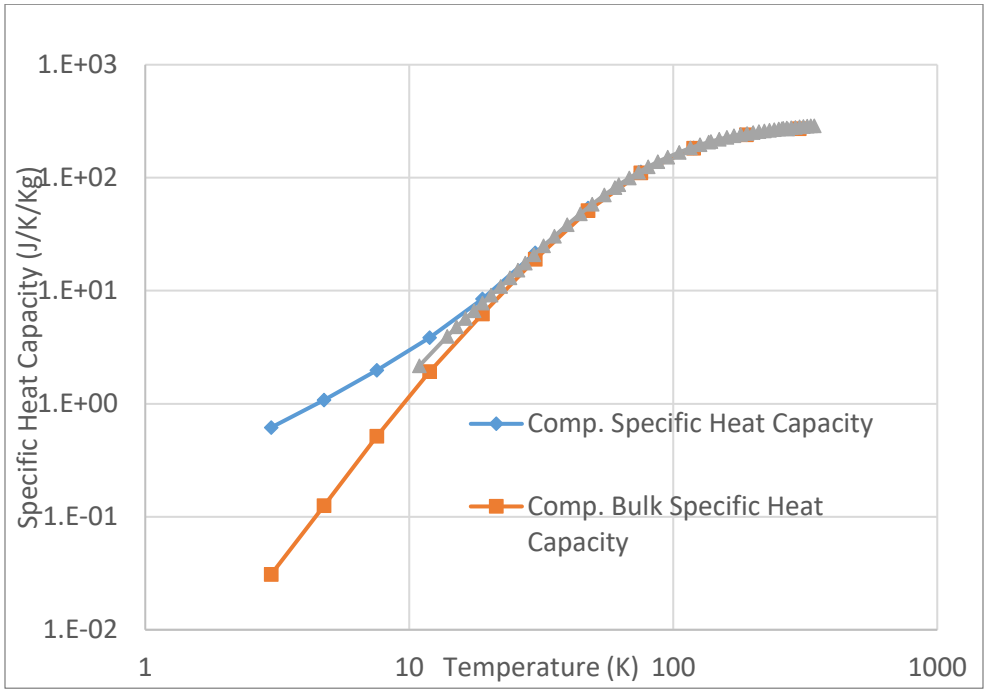

Figure S8: Numerical evaluation of the $MoSe_2$ monolayer specific heat as a function of temperature (blue line). We compare the result with the numerical estimate of the specific heat of $MoSe_2$ bulk and the measured specific heat of $MoSe_2$ bulk (grey line) [18].

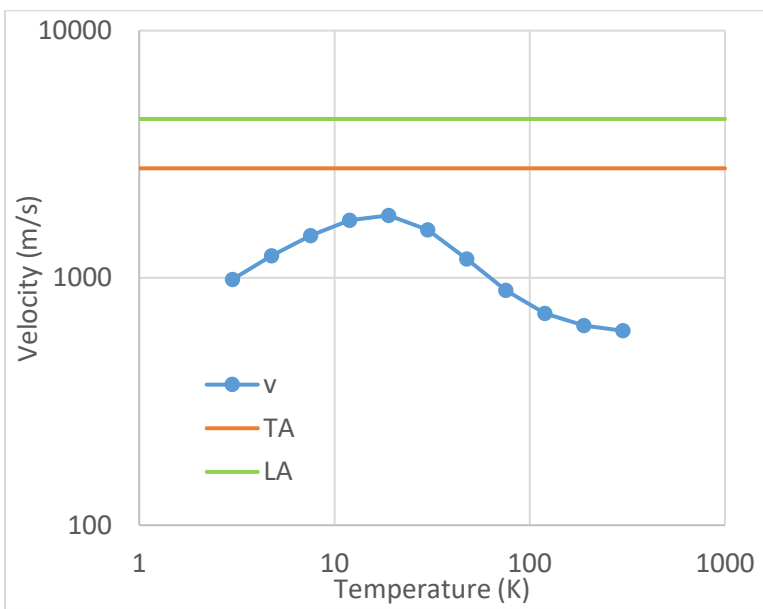

Figure S9: Numerical estimate of the average velocity v (Eq. S44) as a function of temperature. We contrast it with the phonon group velocities of transversal and longitudinal acoustic modes (TA, LA). The average velocity v is lowered by the contribution of the out-of-plane acoustic mode.

Now, we discuss heat capacity. Above, we introduced the equivalent heat capacity where we evaluated

$$P = \frac{\Delta E_{\text{monolayer}}}{\tau} \tag{S45}$$

We take into account that temperature profile is not constant over the membrane, so that

$$P\tau = \int_0^{2\pi} d\theta \int_0^{R_0} r\, dr\, \Delta E_{\text{monolayer}}(r) = 2\pi \int_0^{R_0} r\, dr\, \frac{C_{\text{model}}}{\pi R_0^2} \Delta T_{\text{laser}}(r) \tag{S46}$$

where C_{model} is the membrane heat capacity evaluated when the temperature is not uniform over the suspended area due to laser absorption. Integrating and using Eqs. S32 and S33, we find

$$\begin{aligned} \frac{P\tau R_0^2}{2C_{\text{model}}} &= \int_0^{r_0} r\, dr\, \Delta T_{\text{laser}}(r) + \int_{r_0}^{R_0} r\, dr\, \Delta T_{\text{laser}}(r) \\ &= (T_{\text{center}} - T_0)\left(\frac{r_0^2}{2} + r_0(R_0 - r_0)\right) \end{aligned} \tag{S47}$$

Using $K_{\text{model}} = P/(T_{\text{center}} - T_0)$, we have

$$C_{\text{model}} = \frac{K_{\text{model}}\tau}{2\frac{r_0}{R_0} - \left(\frac{r_0}{R_0}\right)^2} \tag{S48}$$

Using $K = \alpha \cdot K_{\text{model}}$ and $C = \tau \cdot K$, we get

$$C = \frac{1}{\beta} \mathrm{C}_{\text{model}} \tag{S49}$$

$$\frac{1}{\beta} = \alpha\left(2\frac{r_0}{R_0} - \left(\frac{r_0}{R_0}\right)^2\right) \tag{S50}$$

We evaluate the specific heat capacity from the measurement of the equivalent heat capacity C using

$$c = \frac{C_{\text{model}}}{\pi R_0^2\, t\, \rho} = \beta \frac{C}{\pi R_0^2\, t\, \rho}. \tag{S51}$$

with $\beta = 0.86$ and $\beta = 0.85$ for the 1.5 μm and 2.5 μm radius drum, respectively.

Numerical methods

Phonon harmonic and anharmonic properties have been calculated from first-principles within density functional perturbation theory [19-24] as implemented in the Quantum-ESPRESSO distribution [25]. We adopted the local-

density approximation and norm-conserving pseudopotentials from the PSLibrary (http://qe-forge.org/gf/project/pslibrary) and a plane-wave cutoff of 100 Ry. The $MoSe_2$ monolayer is simulated in a slab geometry, with lattice parameter *a*=3.25 Å and a cell height *c*=6*a*. The Brillouin zone is integrated using a Gamma-centered Monkhorst pack of 24x24x1 points for the electronic structure, 16x16x1 for harmonic phonon properties and 6x6x1 for anharmonic force constants. Phonon properties are then Fourier-interpolated to a finer mesh of 128x128x1 points in order to compute thermal properties. A gaussian smearing of 2 cm^{-1} has been used for computing the diffusive thermal conductivity. Finally, the thickness of the $MoSe_2$ membrane is taken as 0.644 nm, equal to the interlayer distance of bulk $MoSe_2$.

References

1. Zhang, X., Sun, D., Li, Y., Lee, G.-H., Cui, X., Chenet, D., You, Y., Heinz, T. F., and Hone, J. C. Measurement of Lateral and Interfacial Thermal Conductivity of Single- and Bilayer MoS_2 and $MoSe_2$ Using Refined Optothermal Raman Technique. *ACS Appl. Mater. Interfaces* **7**, 25923 (2015).

2. Morell, N., Reserbat-Plantey, A., Tsioutsios, I., Schädler, K. G., Dubin, F., Koppens, F. H., and Bachtold, A. High quality factor mechanical resonators based on WSe2 monolayers. *Nano Lett.* **16**, 5102-5108 (2016).

3. Balandin, A. A., Ghosh, S., Bao, W., Calizo, I., Teweldebrhan, D., Miao, F., & Lau, C. N. Superior thermal conductivity of single-layer graphene. *Nano Lett.* **8**, 902-907 (2008).

4. Cai, W., Moore, A. L., Zhu, Y., Li, X., Chen, S., Shi, L., & Ruoff, R. S. Thermal transport in suspended and supported monolayer graphene grown by chemical vapor deposition. *Nano Lett.* **10**, 1645-1651 (2010).

5. Yan, R., Simpson, J. R., Bertolazzi, S., Brivio, J., Watson, M., Wu, X., & Xing, H. G. Thermal conductivity of monolayer molybdenum disulfide obtained from temperature-dependent Raman spectroscopy. *ACS nano* **8**, 986-993 (2014).

6. Ghosh, S., Bao, W., Nika, D. L., Subrina, S., Pokatilov, E. P., Lau, C. N., & Balandin, A. A. Dimensional crossover of thermal transport in few-layer graphene. *Nature Mat*. **9**, 555-558 (2010).

7. Faugeras, C., Faugeras, B., Orlita, M., Potemski, M., Nair, R. R., & Geim, A. K. Thermal conductivity of graphene in corbino membrane geometry. *ACS nano* **4**, 1889-1892 (2010).

8. Lee, J. U., Yoon, D., Kim, H., Lee, S. W., & Cheong, H. Thermal conductivity of suspended pristine graphene measured by Raman spectroscopy. *Phy. Rev. B* **83**, 081419 (2011).

9. Sledzinska, M., Graczykowski, B., Placidi, M., Reig, D. S., Sachat, A. E., Reparaz, J. S., Alzina, F., Mortazavi, B., Quey, R., Colombo, L., Roche, S., & Sotomayor, C. M. Record Low Thermal Conductivity of Polycrystalline MoS2 Films: Tuning the Thermal Conductivity by Grain Orientation. *2D Materials* **3**, 035016 (2016).

10. Metzger, C. H., & Karrai, K. Cavity cooling of a microlever. *Nature* **432**, 1002-1005 (2004).

11. Timoshenko S. P. & Goodier. Theory of Elasticity. 3rd Ed. McGraw Hill (2010).

12. Fugallo G., Lazzeri M., Paulatto L., & Mauri F. Ab Initio Variational Approach for Evaluating Lattice Thermal Conductivity. *Phys. Rev B* **88**, 045430 (2013).

13. Fugallo, G., Cepellotti, A., Paulatto, L., Lazzeri, M., Marzari, N. and Mauri, F. Thermal Conductivity of Graphene and Graphite: Collective Excitations and Mean Free Paths, *Nano Lett*. **14**, 6109-6114 (2014).

14. Paulatto L., Mauri F., & Lazzeri M. Anharmonic Properties from a Generalized Third-Order Ab Initio Approach: Theory and Applications to Graphite and Graphene. *Phys. Rev. B* **87**, 214303 (2013).

15. Garg J., Bonini N., Kozinsky B., & Marzari N. Role of Disorder and Anharmonicity in the Thermal Conductivity of Silicon-Germanium Alloys: A First-Principles Study. *Phys. Rev. Lett.* **106**, 045901 (2011).

16. Ziman J. Electrons and Phonons: The Theory of Transport Phenomena in Solids, Oxford University Press, New York. (2001).

17. Cepellotti, A. & Marzari, N. Boltzmann Transport in Nanostructures as a Friction Effect. Nano Letters 17, 4675 (2017).

18. Kiwia, H. L, and Westrum, E. F. Low-temperature heat capacities of molybdenum diselenide and ditelluride. The Journal of Chemical Thermodynamics, **7**, 683 (1975).

19. Baroni S., de Gironcoli S., Dal Corso A., & P. Giannozzi Phonons and Related Crystal Properties from Density-Functional Perturbation Theory, *Rev. Mod. Phys.* **73**, 515 (2001).

20. Giannozzi P., S. de Gironcoli S., Pavone P., & Baroni S. Ab Initio Calculation of Phonon Dispersions in Semiconductors, *Phys. Rev. B* **43**, 7231 (1991).

21. Debernardi A., Baroni S., & Molinari E. Anharmonic Phonon Lifetimes in Semiconductors from Density- Functional Perturbation Theory. *Phys. Rev. Lett.* **75**, 1819 (1995).

22. Lazzeri M. and de Gironcoli S. First-Principles Study of the Thermal Expansion of Be(1010), *Phys. Rev. B* **65**, 245402 (2002).

23. Baroni S., Giannozzi P., & Testa A. Green's-Function Approach to Linear Response in Solids, *Phys. Rev. Lett.* **58**, 1861 (1987).

24. Gonze X. & Vigneron J. P. Density-Functional Approach to Nonlinear-Response Coefficients of Solids. *Phys. Rev. B* **39**, 13120 (1989).

25. Giannozzi P., Baroni S., Bonini N., Calandra M., Car R., Cavazzoni C., Ceresoli D., Chiarotti G.L., Cococcioni M., Dabo I. et al. QUANTUM ESPRESSO: A Modular and Open-Source Software Project for Quantum Simulations of Materials. *J. Phys. Condens. Matter* **21**, 395502 (2009).